Surface & Coatings Technology 462 (2023) 129462

Contents lists available at ScienceDirect

Surface & Coatings Technology

journal homepage: www.elsevier.com/locate/surfcoat

Cr-containing diamond-like carbon coatings deposited on 316 stainless steel substrates: Characterization and interfacial fracture toughness measurements

N.J. Anderson [a], Bin Zhang [a], A.C. Meng [b], Xiaoman Zhang [a], K.P. Lijesh [a], M.M. Khonsari [a], W.J. Meng [a,*]

[a] Mechanical and Industrial Engineering Department, Louisiana State University, Baton Rouge, LA 70803, USA
[b] Department of Physics and Astronomy, University of Missouri, Columbia, MO 65211, USA

ARTICLE INFO

Keywords:
ICP assisted reactive sputtering
Structural and mechanical characterization
Fracture toughness by microcantilever bending
Dependence of interfacial toughness on crack path

ABSTRACT

A series of Cr-containing hydrogenated amorphous carbon (a-C:H:Cr) coatings were deposited onto 316 stainless steel (316SS) substrates using inductively coupled plasma assisted reactive sputter deposition. Elemental Cr interlayers with different thicknesses of 100, 200, and 300 nm were deposited between a-C:H:Cr and 316SS. Detailed composition, structure, and mechanical behavior characterization of deposited a-C:H:Cr/Cr/316SS specimens were performed. Fracture toughness values of the a-C:H:Cr layer, the Cr layer, and the a-C:H:Cr/Cr/316SS interfacial regions were measured by bending of microcantilever beams with focused ion beam milled pre-notches in-situ a scanning electron microscope. Measured fracture toughness of a-C:H:Cr/Cr/316SS interfacial regions exhibits an approximately linear correlation with the area fraction of the fracture surface occurring in the Cr interlayer, indicating that the interfacial fracture toughness depends on the detailed path of crack propagation and suggesting that interfacial toughness can be engineered through materials design of the interfacial region.

1. Introduction

Application of thin ceramic coatings, typically 1–10 μm in thickness, onto metallic substrates has become an essential tool for achieving the desired load-carrying capacity and tribological performance in harsh environments [1,2]. Prominent examples include coatings for macro machining tools [3,4], micro molding and machining tools [5–8], and mechanical components [9,10]. Mechanical failures of the coating/substrate interfacial region typically led to critical failures of the entire coated system and the component that is designed to protect. Thus, quantitative evaluation of the mechanical response of interfacial regions between thin hard coatings and substrates has remained to be of significant research interest over the last three decades.

Many macroscale mechanical testing techniques have been developed to evaluate mechanical responses of interfaces between thin coatings and substrates. The tensile pull-off test utilizes a polymeric glue to attach an actuator to the surface of a coating/substrate assembly and obtains a tensile strength when a relevant interface fails in tension [11]. This test is incapable of failing strong interfaces due to the strength limitations of the glue layer [12,13]. Even though the scratch test is widely used in industrial settings to rank coating/substrate adhesion [14], the complex contact conditions between the scratch indenter and the coating/substate system frustrate attempts to obtain basic and quantitative interfacial mechanical response data from such a measurement [15]. Several techniques have been employed to quantify the interfacial mechanical response of hard coatings on ductile substrates by imposing a surface strain on the substrate, including the Brale indentation test [16], the substrate tension test [17], and the multi-strain flexture test [18]. The Brale indentation test imposes a compressive surface strain on a ductile substrate via a deep indentation through the coating layer and into the substrate. Although a quantitative measurement of the toughness of a diamond/Ti interface has been achieved [19], only an upper bound can be estimated for high-toughness interfaces where coating spallation does not extend beyond the perimeter of the Brale indentation. The substrate tension test imposes a tensile surface strain on a ductile substrate and obtains an estimate of the limiting shear strength of the coating/substrate interface through measurement of the saturation transverse crack density. The sensitivity of this technique to

* Corresponding author.
E-mail address: wmeng1@lsu.edu (W.J. Meng).

https://doi.org/10.1016/j.surfcoat.2023.129462
Received 16 February 2023; Received in revised form 23 March 2023; Accepted 23 March 2023
Available online 1 April 2023

the residual stress within the coating [20] makes estimating the limiting interfacial shear strength rather imprecise, e.g., the method is unable to distinguish between the same coating/substrate combination when different adhesion-promoting interlayers are used [21]. The multi-strain flexture test imposes in one test varying levels of tensile and compressive surface strains on different coating strips on the side of a beam under four-point bending. In essence, it executes a Brale indentation test and a substrate tension test simultaneously, and therefore suffers from the same limitations of these two tests [22].

Diamond-like carbon (DLC) coatings encompass both hydrogen-free and hydrogenated amorphous carbon with varying bonding configurations, usually denoted as a-C and a-C:H, respectively. Various metals can be incorporated into DLC, forming a-C:Me or a-C:H:Me. These coatings have been intensely studied and widely employed in industrial and commercial applications [23]. One example illustrating the importance of understanding and controlling the mechanical integrity of coating/substrate interfaces is furnished by the application of DLC coatings onto gear systems. Under high-stress, high-cycle contact typically experienced by gear surfaces, some DLC/adhesion-interlayer/steel gear systems can survive millions of contact cycles without interfacial failure while other DLC coated gears with different design of adhesion interlayers suffer massive interfacial spallation [9]. Testing of high-toughness DLC/steel interfaces by Brale indentation and multi-strain flexture yielded only lower bounds on the interfacial toughness [22], making a quantitative assessment of better or worse performing interfaces difficult and motivating further quantitative measurements and materials-based understanding of how to effectively engineer interfaces with improved mechanical integrity.

More recent advances in mechanical testing techniques for interfaces between thin coatings and substrates stem mainly from the development of the capability for site-selective fabrication of micron sized specimens through focused ion beam (FIB) nanoscale machining [24] and the capability for instrumented nano/micro mechanical actuation in-situ scanning electron microscopes (SEMs) [25]. Instrumented meso/micro scale mechanical testing in-situ SEMs under different loading conditions, including compression and tension of meso/micro scale pillars and bending of meso/micro scale cantilever beams, have all been realized [26]. In particular, the use of microscale cantilever bending for toughness measurement has received much attention [27]. Microscale cantilever bending has been employed to measure the fracture toughness of micron-thick WC coating layers [28], as well as the fracture toughness of interfaces between SiO_2 and various metals [29]. With FIB nanoscale milling, pre-notches can be reliably cut into the interface location of interest. As compared to macroscale techniques such as the brale indentation test and the multi-strain flexture test, where uncharacterized initial crack(s) is(are) presumed to initiate from underneath the brale indenter or edges of deposited coating strips, such meso/micro scale testing offers a greater degree of controllability. Testing in-situ SEMs further enables more detailed observations of the specimen post-deformation/fracture.

Extensive development of the mechanics of interfacial fracture exists in the literature [30]. Two decades ago, Evans, Hutchinson, and Wei stated that "a relative paucity of systematic experimental results for interfaces have impeded validation of the ideas and models" [31]. The recent microscale testing protocols listed above enable more quantitative interfacial mechanical response data to be obtained. For example, Schaufler et al. measured the strength and toughness of interfaces between a-C:H and steel substrate using FIB milled microscale cantilever bending with and without FIB cut pre-notch, and obtained both a fracture strength in bending and fracture toughness for a-C:H/steel interfaces with two different Cr interlayer designs [32]. Nonetheless, additional quantitative data on interfacial mechanical response, especially those linking measured mechanical response to interfacial structure and composition, remain in need in order to better understand factors controlling interfacial mechanical response, ultimately leading to genuine materials-based designs for the mechanical integrity of interfaces.

In the present study, we deposited chromium-containing hydrogenated amorphous carbon (a-C:H:Cr) coatings on 316 stainless steel (316SS) substrates by inductively coupled plasma (ICP) assisted vapor phase deposition. Elemental Cr interlayers with different thicknesses of 100, 200, and 300 nm were deposited between a-C:H:Cr and 316SS. Composition, structure, and mechanical properties of deposited a-C:H:Cr/Cr/316SS specimens were characterized in detail. Measurements of the toughness of the a-C:H:Cr/Cr/316SS interfacial regions were carried out via microscale cantilever bending. Microcantilever beams were fabricated from a-C:H:Cr/Cr/316SS specimens through FIB milling, with FIB milled pre-notches placed in the Cr interlayer. The effect of varying the Cr interlayer thickness on the measured interfacial fracture toughness was examined. The fracture toughness values of the a-C:H:Cr coating and the Cr layer were also measured. The present results suggest that the detailed path of interfacial crack propagation plays an important role in determining the effective interfacial fracture toughness.

2. Experimental procedures

Flat 316SS sheets, ~1 mm in thickness, were used as substrates for vapor deposition. Prior to deposition, the 316SS sheets were sequentially polished with 400, 600, 800, 1000, and 1200 grit sandpaper, followed by additional sequential polishing with 6 μm, 3 μm, and 1 μm diamond powders. After polishing, the substrates were cleaned with acetone and methanol, dried, and loaded into the deposition system. An elemental Cr layer was deposited between the a-C:H:Cr coating and the 316SS substrate as Cr is known empirically to be an effective adhesion promotor [31].

Sputter depositions occurred in a vacuum chamber with a base pressure below 1.3×10^{-5} Pa. Seventy-five mm diameter balanced magnetron sources were used with elemental Cr (99.9 %+) targets. A 50 sccm Argon gas (99.999 %+) input flow brought the working pressure to ~0.67 Pa. An Ar ICP was ignited within the deposition chamber using two planar spiral Cu induction coils outside the deposition chamber, coupled to the atmosphere inside the deposition chamber through two facing glass windows. The two Cu induction coils were powered by two separate 13.56 MHz radio frequency power supplies, with the total input power on each supply set to 500 W. The presence of this ICP elevates the plasma density inside the deposition chamber by at least one order of magnitude as compared to that for balanced magnetron sputtering without plasma assist [33,34]. The 316SS substrates were first etched in the Ar ICP for ~5 min, with a − 50 V bias applied. Immediately after substrate etching, the Cr interlayer was deposited in the dc mode with a cathode current of 0.80 A, at a substrate bias of −50 V under the same total ICP input power of 1000 W. With the substantially increased plasma density, the brief Ar ICP substrate etch produced a uniform Cr/316SS interface without indication of remaining oxides/contaminants (see Fig. 2 below). The a-C:H:Cr layer deposition commenced following Cr interlayer deposition. During a-C:H:Cr deposition, the Cr cathode current was reduced to 0.40 A, the substrate bias was increased to −150 V, and a 5.0 sccm C_2H_2 input flow was introduced into the system. The ICP input power was varied between 1000 W and 1200 W to keep the substrate bias current approximately a constant, resulting in an a-C:H:Cr deposition rate of ~700 nm/h. The substrate holder was connected to a 10 RPM stepping motor. The durations of Cr and a-C:H:Cr depositions were varied, respectively, to control the thicknesses of the Cr interlayer and the a-C:H:Cr layer. a-C:H:Cr/Cr/316SS specimens were fabricated with Cr interlayer thicknesses of 100, 200, and 300 nm and an a-C:H:Cr layer of 2.5–3.0 μm in thickness. An elemental Cr film of ~2.5 μm in thickness was deposited separately using the same deposition parameters as those used for the Cr interlayers.

The presence of intended elements and impurities within deposited coating layers were determined using a Scienta Omicron ESCA 2SR X-ray Photoelectron Spectroscope (XPS). A monochromatic Al Kα excitation source was used. XPS spectra were acquired from coating layer

surfaces, either in the as-deposited state after removal from the deposition system or after ion sputter etching with a 5 kV 10 mA Ar^+ ion beam for 20–40 min. Survey scans in the binding energy range of 0–1200 eV in 1 eV steps were acquired immediately after ion etching. Raw XPS data were processed using CasaXPS. Transmission electron microscopy (TEM) characterization was conducted on as-deposited a-C:H:Cr/Cr/316SS cross-sectional specimens using a spherical aberration probe-corrected ThermoFisher Spectra 300 Scanning/Transmission Electron Microscope (S/TEM) operated at 300 kV. The microscope is equipped with a Super-X EDS silicon drift detector system with a 0.7 sr solid angle. Cross-sectional TEM imaging, selected area diffraction patterns (SADPs), and STEM-EDS mapping were conducted. TEM cross-section samples were lifted out using a FEI Quanta 3D DualBeam FEG Ga^+ focused ion beam/scanning electron microscope (FIB/SEM) with final thinning performed at 5 kV. X-ray diffraction (XRD) characterization was carried out using a PANalytical Empyrean system with Cu Kα radiation. Symmetric θ/2θ XRD patterns were collected, and XRD data were analyzed with the PANalytical HighScore™ software packages.

Instrumented nanoindentation was carried out on an MST Nano-Indenter XP instrument with a diamond Berkovich indenter. An indenter tip radius between 150 and 200 nm was determined through calibrations following the Oliver-Pharr procedure. Hardness and indentation modulus were measured as a function of the indentation depth. The indentation modulus is $E/(1-\nu^2)$, where E and ν are respectively the Young's modulus and the Poisson's ratio [35]. Ten repeat measurements were conducted at each load/indentation depth. Evaluation of sliding friction and wear characteristics was conducted with a pin-on-disk setup on a Bruker Universal Mechanical Tester (UMT) instrument. Dry sliding occurred between uncoated and Cr-DLC coated 316SS coupons and 304 stainless steel balls of diameters ranging from 3 to 12.6 mm, at linear velocities ranging from 0.15 to 0.50 m/s. At normal loads ranging from 1.5 to 10 N, the nominal Hertzian contact pressures ranged from 0.45 to 2.18 GPa.

Microcantilever beam specimens were fabricated with FIB milling on the Quanta 3D FIB/SEM. One set of microcantilever beams consisting entirely of the a-C:H:Cr coating layer was fabricated to determine the fracture toughness of the Cr-DLC. Another set of microcantilever beams was fabricated entirely out of a ~ 2.5 μm thick elemental Cr layer deposited onto a 316SS substrate following the same procedure used for depositing Cr interlayers between the a-C:H:Cr layer and the 316SS substrate. A third set of microcantilever beams was fabricated to reveal the a-C:H:Cr/Cr/316SS interfacial region, with FIB milled pre-notches located within the Cr interlayer. The dimensions of as-fabricated microcantilever beams were determined through high resolution SEM imaging on a ThermoFisher Helios™ G4 Xe + plasma focused ion beam/scanning electron microscope system (PFIB/SEM).

Bending of the microcantilever beams was conducted in-situ the Quanta 3D FIB/SEM using a FemtoTools NMT-04 system, using either a ~ 1 μm diameter Si punch or a ~ 2 μm × 2 μm Si punch. The load force, punch displacement, and a SEM video of the microcantilever beams under bending load were recorded. Loading proceeded in displacement control, with displacement rates ranging from 20 nm/s to 50 nm/s. High resolution images of microcantilever beam fracture surfaces were taken using the Helios™ G4 PFIB/SEM. X-ray energy dispersive spectroscopy (EDS) maps of fracture surfaces were collected using an Oxford system housed on the PFIB/SEM. Area measurements on SEM images of microcantilever beam fracture surfaces were conducted using the National Institutes of Health software ImageJ.

3. Results and discussion

3.1. Characterization

Fig. 1 shows the results of the compositional characterization of a-C:H:Cr/Cr/316SS specimens by XPS. Fig. 1(a) and (b) show respectively two XPS spectra collected from the top surface of one a-C:H:Cr layer, in the as-deposited state and after Ar^+ ion etching. O 1s signal is present in the as-deposited state, which decreases to background level after ion etching. N 1s and Ar 2p signals are close to background level in the as-deposited state, but increase after ion etching. Fig. 1(c) shows one XPS spectrum collected from the top surface of another elemental Cr layer deposited onto a 316SS substrate, after Ar^+ ion etching. Only signals from Cr core levels and Auger transitions are present. Data shown in Fig. 1 indicate that O and N impurities within the present series of a-C:H:Cr/Cr/316SS specimens are below the XPS detection limit, ~1 at.% and that no significant impurities are detected near the top of the Cr interlayer.

Fig. 2 shows results of structural characterization of a-C:H:Cr/Cr/316SS specimens by TEM/STEM and XRD. Fig. 2(a) shows a cross-sectional TEM image of one a-C:H:Cr/Cr/316SS specimen, in which the 316SS substrate, the Cr interlayer, and the a-C:H:Cr top layer are shown clearly. The thickness of the Cr interlayer is ~200 nm. Selected area electron diffraction patterns are collected from the 316SS substrate, the Cr interlayer, and the a-C:H:Cr top layer regions and shown respectively in Fig. 2(b), (c), and (d), with placements of the selected area aperture indicated approximately by the red circles marked 1, 2, and 3 in Fig. 2(a). The SADP displayed in Fig. 2(b) shows crystalline diffraction spots from the 316SS substrate. The SADP displayed in Fig. 2(c) shows an indexed polycrystalline ring pattern consistent with that arising from BCC Cr, as expected. The SADP displayed in Fig. 2(d) shows polycrystalline diffraction rings superimposed on a diffuse background. While the diffuse background is consistent with the expected amorphous structure of a-C:H, the three diffraction rings present in Fig. 2(d) correspond to d-spacings that can be consistent with those arising from

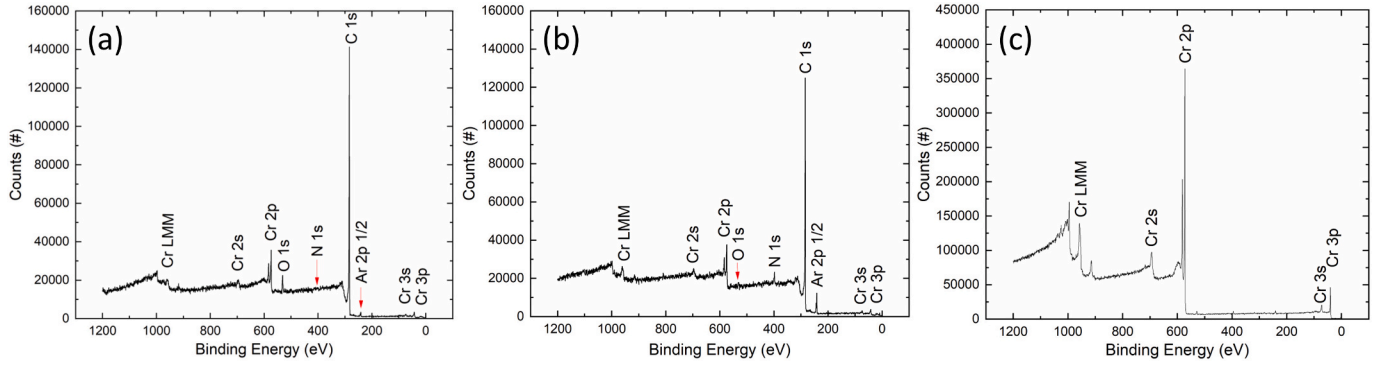

Fig. 1. Compositional characterization of a-C:H:Cr/Cr/316SS specimens: (a) an XPS spectrum acquired from the top surface of one a-C:H:Cr layer in the as-deposited state; (b) an XPS spectrum of the same a-C:H:Cr layer after Ar^+ ion sputter etching. The red arrows in (a) and (b) highlight respectively spectral locations for O 1 s, N 1 s, and Ar 2p; (c) an XPS spectrum acquired from the top surface of one Cr layer deposited on 316SS after Ar^+ ion sputter etching. (For interpretation of the references to colour in this figure legend, the reader is referred to the web version of this article.)

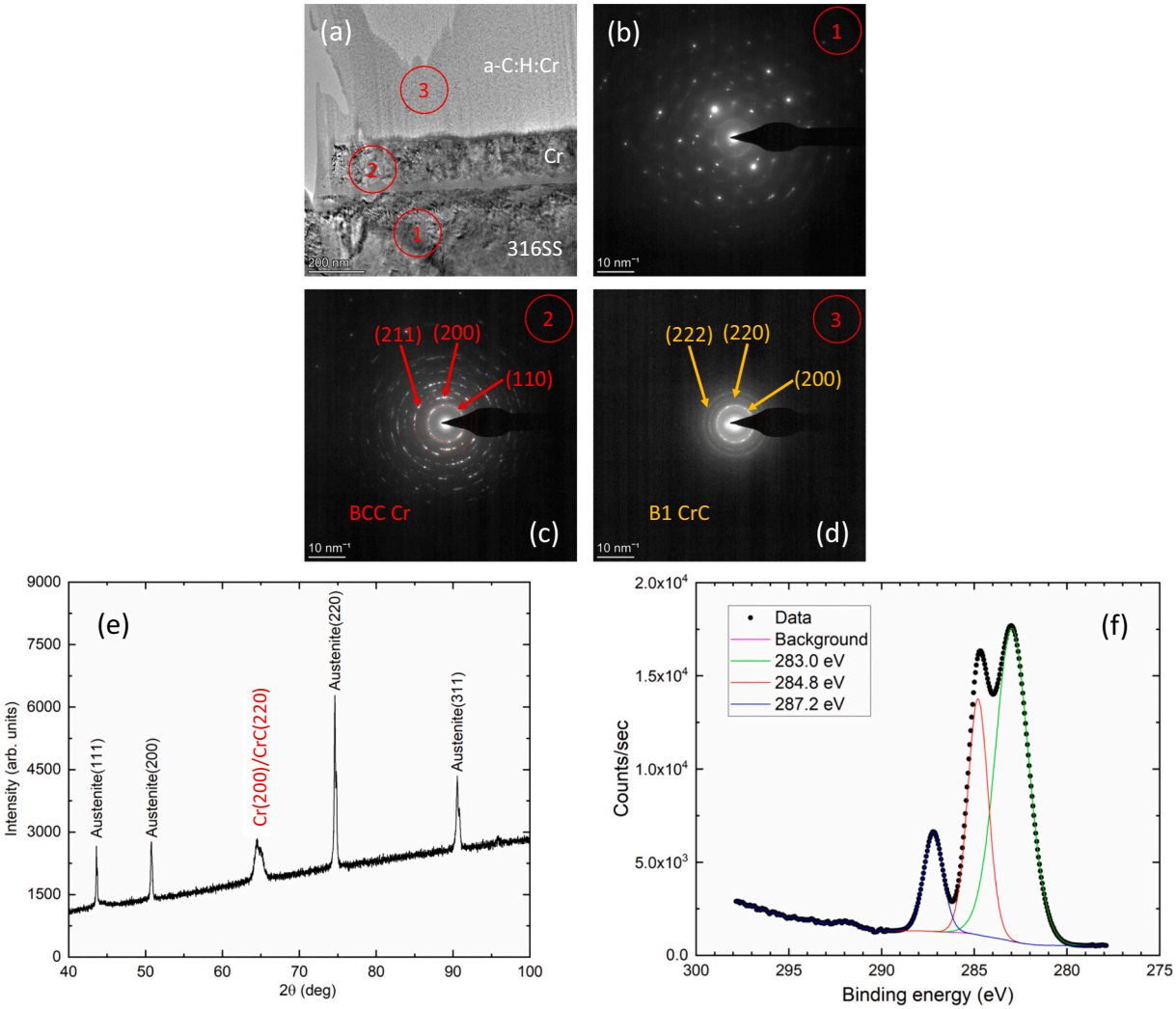

Fig. 2. TEM and XRD characterization of Cr-DLC coated 316SS: (a) cross-section TEM image; (b/c/d) SADPs obtained respectively from the 316SS substrate, Cr interlayer, and a-C:H:Cr layer regions. The placement of the SAD apertures is indicated approximately by the red circles 1, 2, and 3 in (a); (e) θ/2θ XRD pattern obtained from one a-C:H:Cr/Cr/316SS specimen with indexed diffraction peaks; (f) a high-resolution XPS spectrum around C 1 s collected from the top surface of the a-C:H:Cr layer in the as-deposited state. (For interpretation of the references to colour in this figure legend, the reader is referred to the web version of this article.)

either BCC Cr (110), (200), and (211) reflections or Rocksalt CrC (200), (220), and (222) reflections [36]. Fig. 2(e) shows a θ/2θ XRD pattern from the a-C:H:Cr/Cr/316SS specimen. Aside from the diffraction peaks indexed to the Austenite structure of the 316SS substrate, the only other crystalline diffraction peak present in the pattern can again be indexed to either BCC Cr (200) or B1 CrC (220). Fig. 2(f) shows a high-resolution XPS spectrum around the C 1 s binding energy, collected from the top surface of the a-C:H:Cr layer in the as-deposited state. The measured C 1 s binding energy profile can be fitted to three components with binding energies of 283.0 eV, 284.8 eV, and 287.2 eV, respectively. While binding energies of 284.8 eV and 287.2 eV are respectively consistent with C—C and C—O bonds, the 283.0 eV component is consistent with C—Cr bonding [37]. The combined diffraction and XPS data suggest that Cr within the a-C:H:Cr layer exists in the form of a metastable B1 CrC.

Fig. 2(a) also shows two thin transition layers at the Cr/316SS and a-C:H:Cr/Cr interfaces, which are devoid of diffraction contrast. Fig. 3 shows the results of cross-section STEM characterization of the a-C:H:Cr/Cr interfacial region. Fig. 3(a) and (b) show respectively cross-section STEM EDS intensity maps of C Kα and Cr Kα. As one traverses from the Cr interlayer (bottom of figure) into the a-C:H:Cr top layer (top of figure), the Cr intensity decreases and gives way to a uniform C intensity, as expected. Fig. 3(c) shows the corresponding cross-section high angle annular dark field (HAADF) STEM image of the a-C:H:Cr/Cr interfacial region. Fig. 3(d) shows the result of quantification of a STEM EDS line scan from within the Cr interlayer region into the a-C:H:Cr top layer region with the line scan path approximately perpendicular to the interface, as indicated by the light blue arrow in Fig. 3(c). The EDS line scan indicates that a compositionally graded transition layer exists at the a-C:H:Cr/Cr interface, with the thickness of the transition layer being ~40 nm. As the ICP was kept on during the entire deposition process, this compositionally graded transition layer can be consistent with ion-induced compositional mixing at the interface, which is accentuated by the much higher ion flux due to the high plasma density of the ICP. The average Cr composition within the a-C:H:Cr layer is ~40 at.% according to the EDS data shown in Fig. 3(d). A similar compositionally mixed region is observed at the Cr/316SS interface.

Fig. 4 shows the results of cross-section STEM characterization of the a-C:H:Cr top layer from a thinner region as compared to the a-C:H:Cr region shown in Fig. 3. Fig. 4(a) and (b) show respectively cross-section STEM EDS intensity maps of C Kα and Cr Kα. While more uniform C Kα and Cr Kα intensities are shown in Fig. 3, Fig. 4(b) shows clear nanoscale Cr clustering. The corresponding cross-section HAADF STEM image is shown in Fig. 4(c), in which nm scale cluster contrast is also present due to Z contrast, consistent with the EDS mapping information shown in

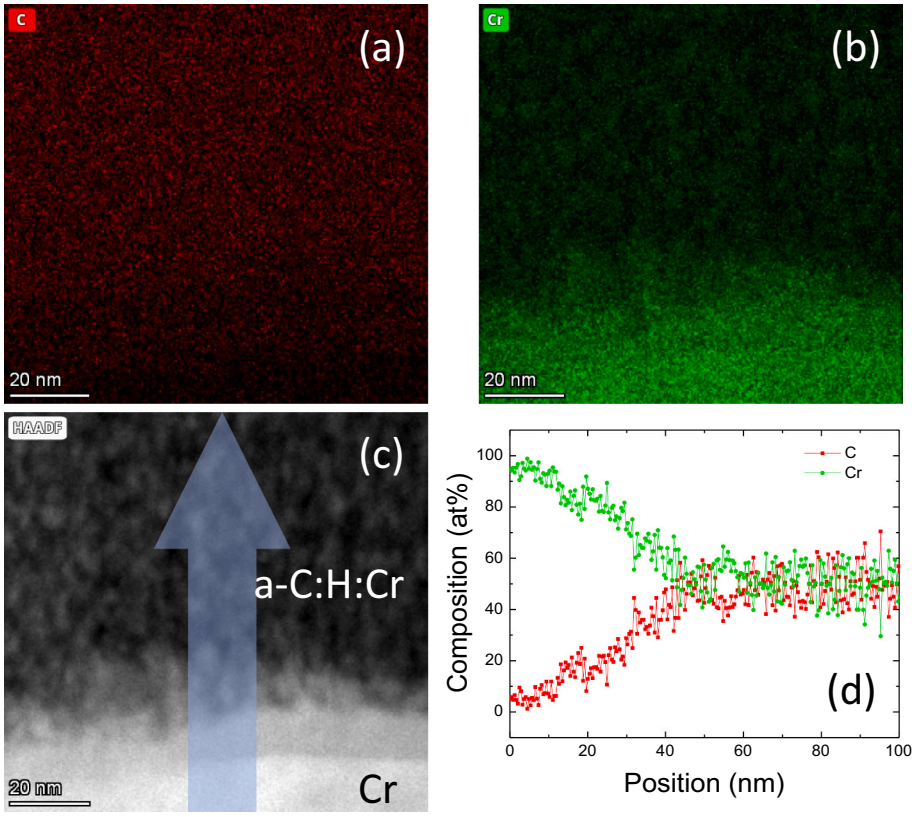

Fig. 3. STEM characterization of interfacial region between the a-C:H:Cr top layer and the Cr interlayer: cross-section STEM EDS intensity map of (a) C; (b) Cr; (c) HAADF cross-section image of the a-C:H:Cr/Cr interfacial region; (d) quantification of STEM EDS line scan, with the line scan path indicated by the light blue arrow in (c). (For interpretation of the references to colour in this figure legend, the reader is referred to the web version of this article.)

Fig. 4(b). Fig. 4(d) shows the result of the quantification of a STEM EDS line scan within the a-C:H:Cr top layer region, with the line scan path indicated by the light blue arrow in Fig. 4(c). Metastable CrC nanoparticles in thicker regions can overlap with each other sufficiently in the electron beam direction to exhibit seemingly uniform average C and Cr composition; this cannot occur when the sample thickness decreases below a threshold. Data shown in Figs. 2 and 4, combined, indicate that the a-C:H:Cr layer consists with nm sized metastable CrC clusters embedded in an a-C:H matrix.

Fig. 5 shows the results of hardness and modulus measurements by instrumented nanoindentation. Fig. 5(a) shows hardness values vs. indentation depth measured from one a-C:H:Cr/Cr/316SS specimen and one uncoated 316SS substrate. Hardness values (H) measured from the uncoated 316SS shows an increase with decreasing indentation depth (h). The inset in Fig. 5(a) shows H^2 plotted vs. $1/h$, the linear proportionality between H^2 and $1/h$ shows the expected indentation size effect on uncoated 316SS. Measured H values for the a-C:H:Cr/Cr/316SS specimen also increases with decreasing h. At small h values, an approximate hardness plateau is reached with an H value of ~7.5 GPa. Fig. 5(b) shows, as a function of the indentation depth, corresponding values of indentation modulus, $E/(1-\nu^2)$. For the uncoated 316SS, measured values of the indentation modulus are close to 225 GPa, consistent with expected values of $E = 205$ GPa and $\nu = 0.3$ for 316SS. For the a-C:H:Cr/Cr/316SS specimen, the measured indentation modulus decreases with decreasing indentation depth, and reaches an approximate plateau with an $E/(1-\nu^2)$ value of ~75 GPa. The values of 7.5 GPa and 75 GPa are taken as being representative of the hardness and indentation modulus of the present a-C:H:Cr or Cr-DLC layer. The fact that the ratio of hardness to modulus for the present Cr-DLC is ~0.1 is also consistent with previous results on Me-DLC coatings [38].

Fig. 6 shows the results of the pin-on-disk evaluation of sliding friction and wear characteristics. The purple trace displaced in Fig. 6(a) show the measured friction coefficient due to dry sliding contact between a 304 stainless steel ball and an uncoated 316SS coupon, at a Hertzian contact pressure of 0.45 GPa and a sliding speed of 0.15 m/s. As a function of time, the friction coefficient exhibits large variations, ranging between 0.6 and 0.8. The red and blue traces in Fig. 6(a) show measured friction coefficients due to dry sliding contact between a 304 stainless steel ball and a Cr-DLC coated 316SS coupon at Hertzian contact pressures of 1.06 and 1.33 GPa, respectively. The presence of the a-C:H:Cr/Cr layers between the 304 stainless steel ball and the 316SS substrate leads to a much lower friction coefficient of ~0.2, with much lower variations. Fig. 6(b) shows an SEM image of the wear track on the uncoated 316SS coupon after a total sliding distance of ~525 m at a Hertzian contact pressure of 0.45 GPa. Without quantifying the wear volume, it is evident from Fig. 6(b) that severe wear has occurred within the wear track, generating a large amount of wear debris that piled up outside the wear track. Fig. 6(c) shows an SEM image of the wear track on the Cr-DLC coated 316SS coupon after a total sliding distance of ~525 m at a normal load of 1.5 N and a Hertzian contact pressure of 0.45 GPa. Figs. 6(d/e/f) shows the corresponding EDS intensity maps of C Kα, Cr Kα, and Fe Kα, respectively. As compared to areas outside the wear track, the Cr Kα and Fe Kα intensity have increased within the wear track, while the C Kα intensity has decreased but not eliminated. Data displayed in Figs. 6(c-f) show that, while wear has occurred, the a-C:H:Cr layer has not been completely removed within the wear track. Taking into account the wear track width measured from Fig. 6(c) of ~180 μm, the thickness of the a-C:H:Cr layer of ~700 nm, and the normal load of 1.5 N, an upper bound on wear rate and wear coefficient can be estimated to be, respectively, 2.1×10^{-5} mm^3/m and $\sim 1.4 \times 10^{-5}$ mm^3/(N m), by assuming the removal of the entire a-C:H:Cr layer within the observed wear track width. This order of magnitude estimate of dry

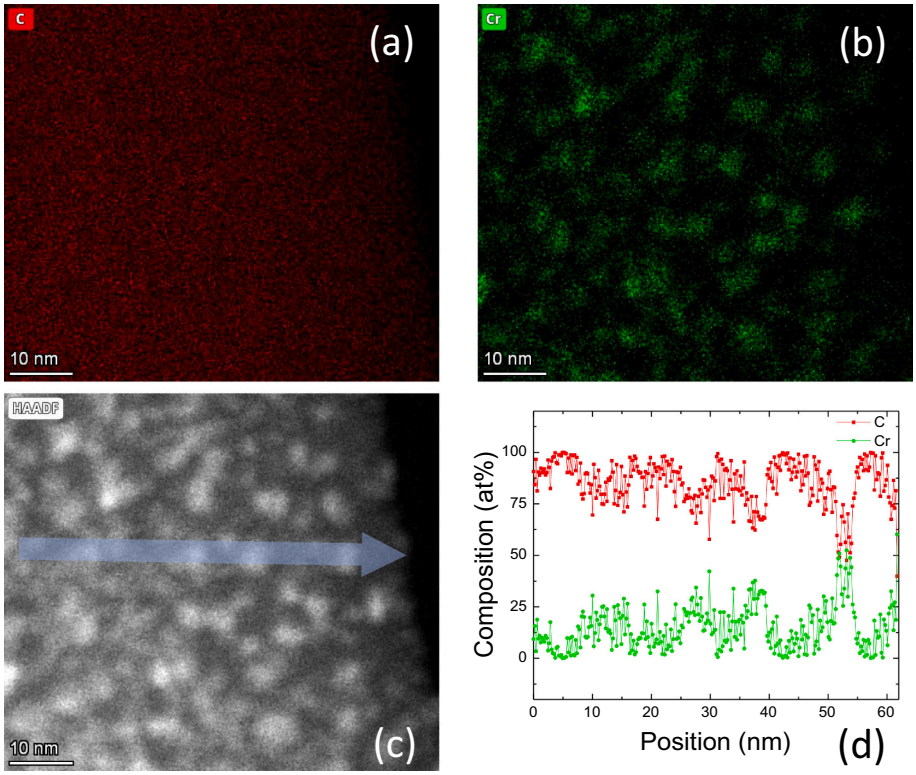

Fig. 4. STEM characterization of the a-C:H:Cr layer: cross-section STEM EDS intensity map of (a) C; (b) Cr; (c) HAADF cross-section image of the a-C:H:Cr layer; (d) quantification of STEM EDS line scan, with the line scan path indicated by the light blue arrow in (c). (For interpretation of the references to colour in this figure legend, the reader is referred to the web version of this article.)

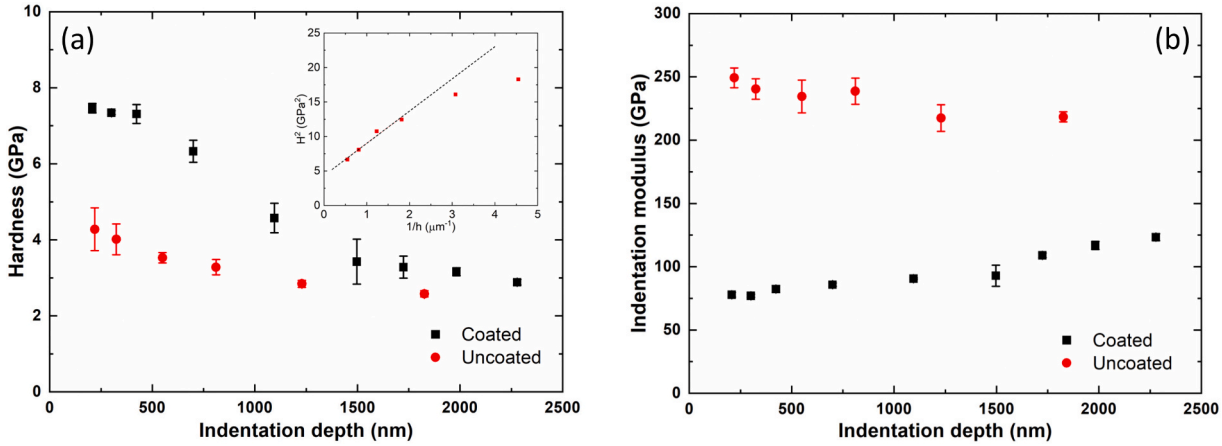

Fig. 5. Instrumented nanoindentation of Cr-DLC coated and uncoated 316SS substrates: (a) hardness and (b) indentation modulus plotted vs. indentation depth. The inset in (a) is a plot of H^2 vs. 1/h for the uncoated 316SS specimen.

sliding wear coefficient is in accordance with previously reported values for Me-DLCs [39]. Data shown in Fig. 6(a) further indicate that gradual wear of Cr-DLC occurred under dry sliding between 304 stainless steel ball and Cr-DLC coated 316SS coupon up to ~1.3 GPa of Hertzian contact pressure without inducing spallation at or failure of the Cr-DLC/substrate interfaces.

3.2. Fracture toughness measurements

Fracture toughness values of the a-C:H:Cr layer, the Cr layer, and the interfacial region between the a-C:H:Cr layer and the 316SS substrate were determined by bending of microcantilever beams with FIB milled pre-notches [40]. Fig. 7 shows typical microcantilever beams fabricated by FIB milling. Fig. 7(a) shows one beam consisting entirely of the a-C:H:Cr layer, with the Cr interlayer and 316SS substrate underneath removed and a pre-notch cut into the beam top surface. It should be noted that, due to the presence of an intrinsic compressive stress within the a-C:H:Cr layer, the remaining a-C:H:Cr cantilever immediately after removal of the Cr interlayer and the 316SS substrate curves slightly. The slightly curved a-C:H:Cr cantilever was milled further after removal of the Cr interlayer and the 316SS substrate to produce beams that were parallel with the original film surface. In this final state of the a-C:H:Cr cantilever, the intrinsic stress has been released.

Fig. 7(b) shows one beam milled with the specimen placed in a 90° rotated orientation, exposing the a-C:H:Cr layer with a thickness of ~3 μm, the Cr interlayer with a thickness of ~300 nm, and the 316SS

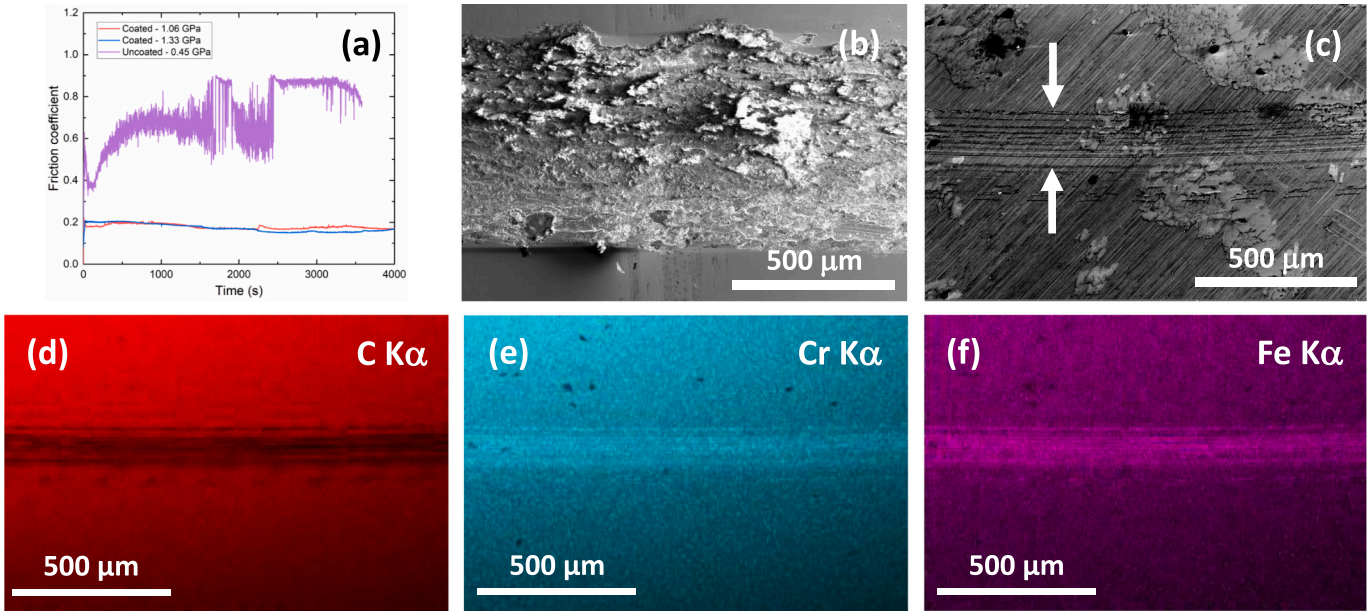

Fig. 6. Dry friction and wear of Cr-DLC coated and uncoated 316SS: (a) sliding friction coefficient of uncoated and Cr-DLC coated 316SS coupons at different contact pressures; (b) an SEM image of the wear track on the uncoated 316SS at 0.45 GPa contact pressure; (c) an SEM image of the wear track on the Cr-DLC coated 316SS at 0.45 GPa contact pressure; (d/e/f) EDS intensity maps of C Kα, Cr Kα, and Fe Kα on the wear track shown in (c). White arrows in (c) highlight the location of the wear track.

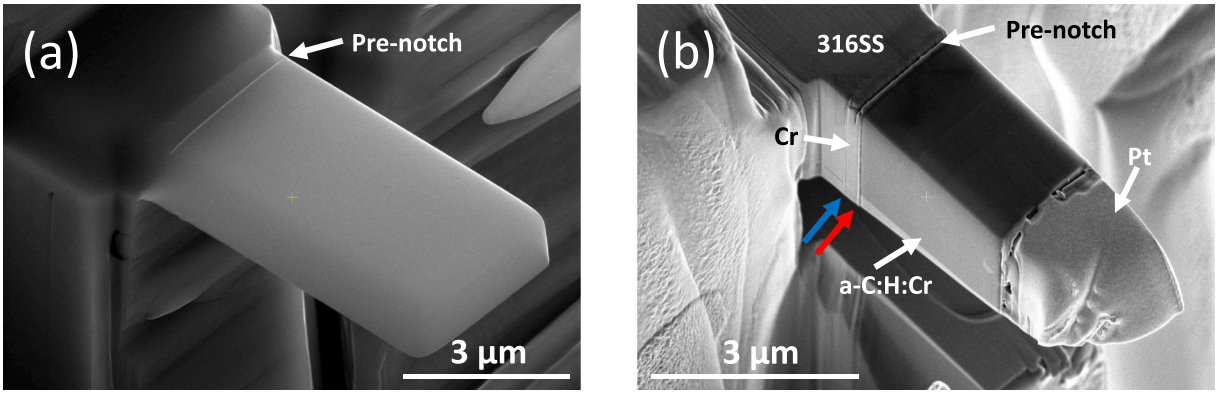

Fig. 7. Microcantilever beams fabricated by FIB milling: (a) one beam milled entirely within the a-C:H:Cr coating layer; (b) one beam exposing the a-C:H:Cr layer, the Cr interlayer, and the 316SS substrate. A FIB milled pre-notch was cut into the top DLC coating surface in (a) and the middle of the Cr interlayer top surface in (b). The blue and red arrows in (b) highlight the locations of the 316SS/Cr and Cr/a-C:H:Cr interfaces. (For interpretation of the references to colour in this figure legend, the reader is referred to the web version of this article.)

substrate. A pre-notch was FIB milled into the middle of the Cr interlayer top surface. A Pt layer was deposited onto the a-C:H:Cr top surface for protection during FIB milling. The protective Pt layer does not influence the bending data as the bending load was applied on a-C:H:Cr. A separate elemental Cr layer, ~3 µm in thickness, was deposited onto a 316SS substrate following the same deposition procedure for Cr interlayers. Separate microcantilevers consisting entirely of the Cr layer were fabricated, analogous to the a-C:H:Cr cantilever shown in Fig. 7(a). Pre-notched Cr microcantilever bending was conducted to measure the fracture toughness of the deposited Cr layer. The microcantilever beam width B and thickness in the loading direction W were measured before the test by averaging a minimum of three measurements taken from SEM images. The depth of the pre-notch a was measured by averaging a minimum of three measurements taken from SEM images of the beam fracture surface after test.

The load-displacement (F-d) curve associated with each beam bending was collected and corrected for force drift during measurement. Fig. 8(a) shows typical F-d curves measured from the bending of pre-notched microcantilever beams. Differences in beam dimensions contribute to variations in force and indenter displacement. For example, beams composed entirely of a-C:H:Cr and Cr have longer load arms as compared to beams exposing the a-C:H:Cr/Cr/316SS interface. It is evident from Fig. 8(a) that the F-d curves associated with bending of pre-notched Cr beams and pre-notched a-C:H:Cr beams are linear up to the point of fracture. The F-d curves associated with the bending of a-C:H:Cr/Cr/316SS beams with pre-notches milled into the middle of the Cr interlayers remain largely linearly up to the point of fracture, see for example three of the four F-d curves shown in Fig. 8(a) with Cr interlayer thicknesses of 100 nm, 200 nm, and 300 nm. Fig. 8(a) also shows an example of exception: the F-d curve (shown in green in Fig. 8(a)) with a Cr interlayer thickness of 200 nm shows a clear deviation from linearity, exhibiting a linear rise in force with displacement followed by a force plateau. Fig. 8(b) shows an SEM image of this particular a-C:H:Cr/Cr/316SS beam after fracture has occurred. The two white arrows highlight

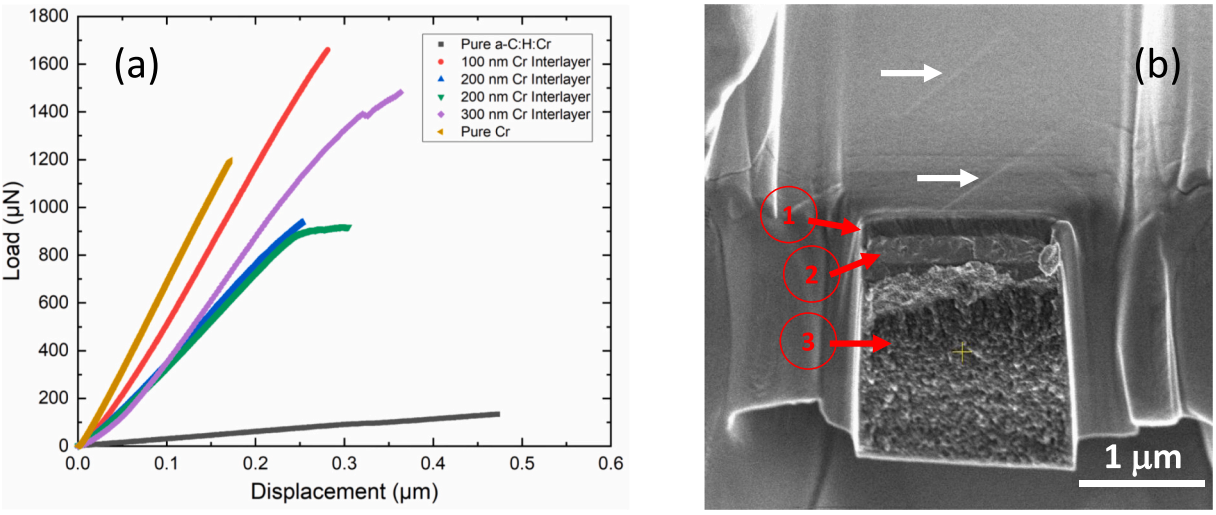

Fig. 8. (a) Typical load-displacement curves measured from pre-notched microcantilever beam bending experiments. Different symbols shown in the legend identify measurements made on a pre-notched Cr beam, a pre-notched a-C:H:Cr beam, and a-C:H:Cr/Cr/316SS beams with pre-notches milled into the middle of the Cr interlayers; (b) SEM image of a fractured a-C:H:Cr/Cr/316SS beam with a 200 nm thick Cr interlayer. The two white arrows highlight the slip traces on the surface of the 316SS substrate formed due to loading of the cantilever in bending. The red arrows marked 1, 2, and 3 denote respectively on the fracture surface the pre-notch, fracture within the Cr interlayer, and fracture within the a-C:H:Cr layer. (For interpretation of the references to colour in this figure legend, the reader is referred to the web version of this article.)

the slip traces on the surface of the 316SS substrate formed due to loading of the cantilever in bending, from which it is concluded that the apparent plasticity exhibited by the *F-d* curve is due to plasticity occurring within the 316SS region, rather than within the interface region where fracture occurred. The presently observed interfacial fractures are consistent with linear elastic fracture mechanics, and plasticity does not dominate the interfacial fracture events. In Fig. 8(b), the FIB milled pre-notch region exhibits a smooth morphology that is easily distinguishable from the fracture surfaces after bending. Propagation of crack initiated from the pre-notch (delineated in Fig. 8(b) by arrow 1) deviated from a straight path, stayed within the Cr interlayer (delineated in Fig. 8(b) by arrow 2) and finished within the a-C:H:Cr layer (delineated in Fig. 8(b) by arrow 3).

Fig. 9 shows typical morphologies of fractured microcantilever beams. Fig. 9(a) shows an SEM image of a typical broken a-C:H:Cr beam. Fracture initiated from the FIB milled pre-notch and remained relatively straight while propagating through the entire beam thickness. Figs. 9(b/c/d) show respectively SEM images of broken a-C:H:Cr/Cr/316SS beams with fractures initiated from pre-notches milled in the middle of the Cr interlayers with thicknesses of 100 nm, 200 nm, and 300 nm. The FIB milled pre-notch regions are easily distinguishable from the rest of the fracture surface due to morphological differences, with the FIB milled regions being smoother. While fractures initiated from the pre-notches, it is noted that they deviated from straight paths and propagated from the Cr layer into the a-C:H:Cr layers as cracks extended. This is confirmed through the SEM EDS mapping shown in Fig. 10. Fig. 10(a) shows an SEM image of the fracture surface of one broken a-C:H:Cr/Cr/316SS microcantilever beam with a Cr interlayer thickness of 200 nm.

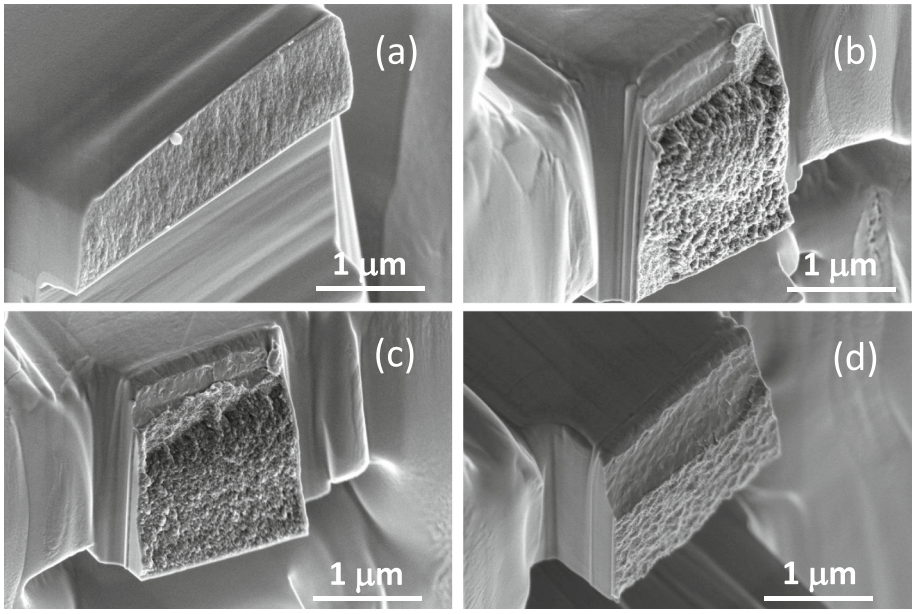

Fig. 9. Typical morphologies of fractured micro cantilever beams with FIB milled pre-notches: (a) a pure a-C:H:Cr beam; (b/c/d) a-C:H:Cr/Cr/316SS beams with fractures initiated from pre-notches cut in the middle of the Cr interlayers of thickness (b) 100 nm; (c) 200 nm; (d) 300 nm.

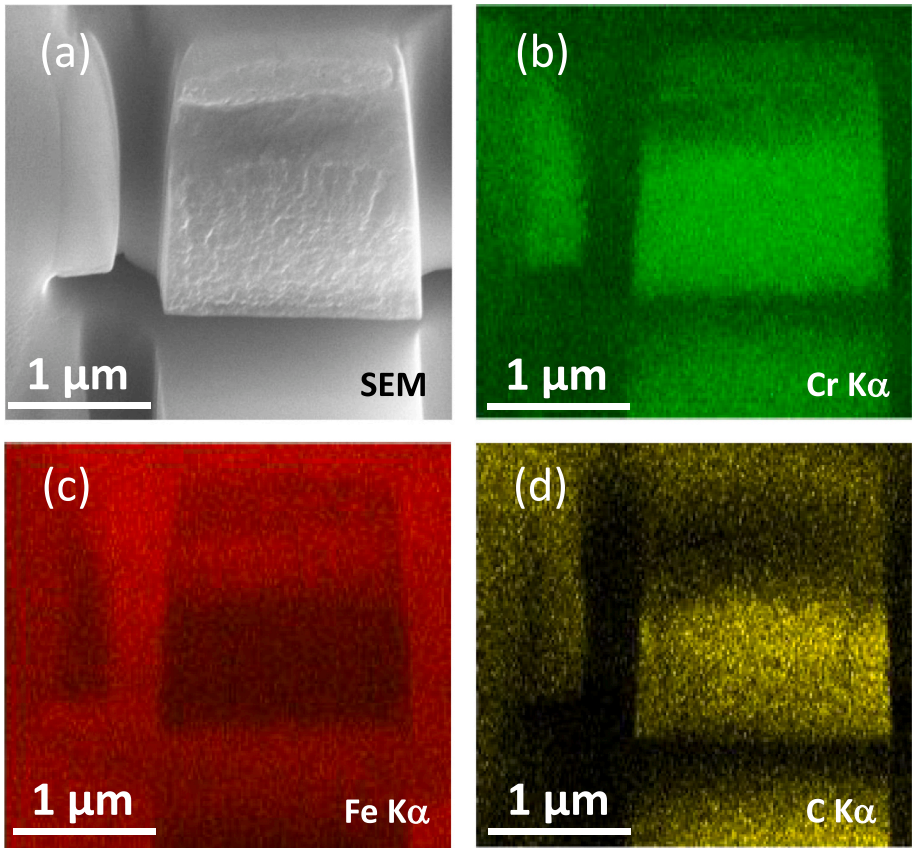

Fig. 10. Typical EDS mapping of the interfacial fracture surface of one a-C:H:Cr/Cr/316SS microcantilever beam: (a) an SEM image of the fracture surface; (b)/(c)/(d) show respectively X-ray intensity maps of Cr Kα, Fe Kα, and C Kα.

Figs. 10(b/c/d) show respectively the associated X-ray intensity maps of Cr Kα; Fe Kα; and C Kα. The Cr Kα and C Kα intensities increase toward the bottom part of the fracture surface while the Fe Kα intensity decreases, consistent with the bottom part of the fracture surface being within the a-C:H:Cr layer.

Following Iqbal et al., the fracture toughness value is obtained from the bending fracture measurement via

$$K_{IC} = \frac{FL}{BW^{\frac{3}{2}}} f\left(\frac{a}{W}\right) \quad (1)$$

where F is the fracture force, L is the load arm length or the distance between loading point and the pre-notch, B and W are respectively the cantilever beam width and thickness, a is the depth of the pre-notch, and $f(a/W)$ is a dimensionless function of a and W [40]. Table 1 shows measured K_{IC} values for the a-C:H:Cr layer, the a-C:H:Cr/Cr/316SS interfaces with varying Cr interlayer thicknesses, and the elemental Cr layer. The measured fracture toughness of Cr, 2.5 MPa $m^{1/2}$, is consistent with previously reported values for ultrafine grain Cr [41]. Fig. 11(a) plots fracture toughness values for a-C:H:Cr/Cr/316SS interfacial regions as a function of the Cr interlayer thickness measured from separate beam bending experiments and illustrates the level of data scatter. Within experimental error, there is not a noticeable trend relating interlayer thickness to measured fracture toughness of the a-C:H:Cr/Cr/316SS interfacial region.

Table 1
Average fracture toughness and standard deviation of tested microcantilever beams.

	K_{IC} (MPa $m^{1/2}$)	Standard deviation (MPa $m^{1/2}$)
a-C:H:Cr	0.80	0.15
a-C:H:Cr/Cr/316SS interface: Cr interlayer thickness 100 nm	2.02	0.36
a-C:H:Cr/Cr/316SS interface: Cr interlayer thickness 200 nm	1.52	0.17
a-C:H:Cr/Cr/316SS interface: Cr interlayer thickness 300 nm	1.91	0.24
Cr	2.50	0.38

3.3. Discussion

Observations documented in Figs. 9 and 10 indicate that fracture did not occur entirely within the Cr interlayer, even though the FIB milled pre-notch was in its center. Fig. 11(b) shows an SEM image of a typical fracture surface, with identification of the areas corresponding to the FIB milled pre-notch, fracture within the Cr interlayer, and fracture within the a-C:H:Cr layer. The software ImageJ was used to determine the projected area fraction of the fracture surface that occurred within the Cr interlayer and the a-C:H:Cr layer. This process was repeated for all broken a-C:H:Cr/Cr/316SS beams. Fig. 11(c) replots data shown in Fig. 11(a) vs. the projected area fraction of fracture surface occurring in the Cr interlayer. The datapoints at fraction values of 0 and 1 correspond respectively to fracture toughness values measured from a-C:H:Cr beams and Cr beams. There is a clustering of data points within projected area fractions between 0.2 and 0.4 and between 0.8 and 0.9. As shown by the red line in Fig. 11(c), measured fracture toughness values of the a-C:H:Cr/Cr/316SS interfacial regions follow an approximately linear correlation with the area fraction, ranging between the fracture toughness of a-C:H:Cr and elemental Cr. The relatively large data scatter notwithstanding, data shown in Fig. 11 suggest that the measured fracture toughness of the interfacial region depends on the detailed path of the crack as it propagates through the specimen.

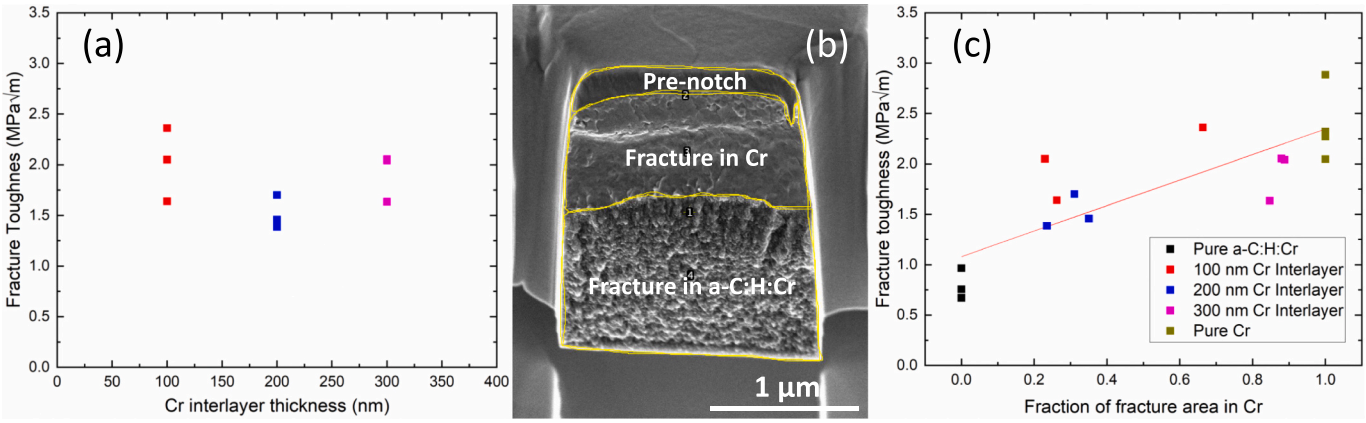

Fig. 11. (a) Measured fracture toughness of the a-C:H:Cr/Cr/316SS interfacial region vs. the thickness of the Cr interlayer; (b) an SEM image of an typical fracture surface, with identification of the areas corresponding to the FIB milled pre-notch, fracture within the Cr interlayer, and fracture withing the a-C:H:Cr layer; (c) data shown in (a) replotted vs. the fraction of fracture area occurring in the Cr interlayer. The data points at fractions of 0 and 1 correspond respectively to fracture toughness values measured from pure a-C:H:Cr beams and pure Cr beams.

Mechanical failures at hetero-material interfaces, including the present case of Cr-DLC/316SS interfaces, are complex because different interfacial mechanical responses are elicited under different loading or contact conditions. When ceramic/metal interfaces are subjected to shear loading, shear failure can occur through either plasticity within the metal or relative sliding at the ceramic/metal interface [42]. Under tensile loading, dislocation activities within the metal can lead to dislocation pileup in front of the ceramic/metal interface, thereby generating excess vacancy concentration, nanovoid nucleation, and eventual tensile interfacial fracture [43,44]. The present results suggest that the effective fracture toughness of ceramic/interlayer/substrate interfacial region may be altered by controlling the path of the crack as it propagates through the interfacial region and by controlling the fracture toughness of the adhesion-promoting interlayer. Thus, engineering the mechanical response of ceramic/interlayer/substrate interfacial region may involve control of bonding interactions between the various materials as well as plasticity and fracture toughness of the interlayer. Furthermore, the microstructure of the interfacial region may exert an influence on the path of crack propagation, e.g., the columnar structure of the Cr interlayer may act to "steer" the crack path away from the original pre-notch direction [45]. Additional investigations are needed to establish effective means of engineering the microstructure of the interfacial region to control the path of interfacial crack propagation. A general approach to these issues does not exist at present and remains the subject of future studies.

4. Summary

Inductively coupled plasma assisted reactive sputter deposition of a-C:H:Cr coatings on 316SS substrates with Cr interlayers of different thicknesses was described. Composition, structure, and mechanical behavior of deposited a-C:H:Cr/Cr/316SS specimens were characterized with XPS, TEM/STEM, EDS, XRD, instrumented nanoindentation and pin-on-disk dry sliding. The a-C:H:Cr layer consists of nm sized metastable CrC particles embedded within an a-C:H matrix. Measured hardness, modulus, friction coefficient and wear rate are consistent with general characteristics exhibited by Me-DLC coatings. Fracture toughness values of a-C:H:Cr, Cr, and a-C:H:Cr/Cr/316SS interfacial regions were measured by bending of pre-notched microcantilever beams in-situ an SEM. Both a-C:H:Cr and Cr microcantilever beams exhibit brittle fracture behavior during bending. The measured fracture toughness value of vapor-deposited Cr is consistent with previous reports on ultrafine grain Cr. Fracture toughness values of the a-C:H:Cr/Cr/316SS interfacial regions were measured at Cr interlayer thicknesses of 100 nm, 200 nm, and 300 nm. An approximately linear correlation was observed between the area fraction of the fracture surface occurring in the Cr interlayer and the measured interfacial fracture toughness.

CRediT authorship contribution statement

Nicholas J. Anderson: Methodology, Data Collection and Curation, Formal analysis, Investigation, Writing – Original Draft, Writing - Review & Editing.

Bin Zhang: Methodology, Data Collection and Curation, Formal analysis, Investigation.

Andrew C. Meng: Methodology, Data Collection and Curation, Formal analysis, Investigation, Writing – Original Draft, Writing - Review & Editing.

Xiaoman Zhang: Methodology, Data Collection and Curation, Formal analysis, Investigation.

K.P. Lijesh: Methodology, Data Collection and Curation, Formal analysis, Investigation.

M.M. Khonsari: Resources, Funding acquisition.

W.J. Meng: Conceptualization, Data Collection and Curation, Validation, Investigation, Resources, Writing – Original Draft, Writing - Review & Editing, Supervision, Project administration, Funding acquisition.

Declaration of competing interest

The authors declare no competing interests in the matter of this manuscript.

Data availability

Data will be made available on request.

Acknowledgements

This work was funded in part by the NSF EPSCoR program, under awards OIA-1541079 and OIA-1946231. Partial project support through an NSF IUCRC, award IIP-2052810, is acknowledged. Use of experimental facilities at the LSU Shared Instrumentation Facility (SIF), a part of the Louisiana Core User Facilities (CUF), is acknowledged. Use of experimental facilities at the MU Electron Microscopy Core (EMC) Facilities is acknowledged.

References

[1] K. Holmberg, A. Matthews, Coatings Tribology: Properties, Mechanisms, Techniques and Applications in Surface Engineering, 2nd Edition, Elsevier Science, 2009.
[2] I. Hutchings, P. Shipway, Tribology: Friction and Wear of Engineering Materials, 2nd edition, Butterworth-Heinemann, Cambridge, Massachusetts, 2017.
[3] T. Scelle, A. Barimani, Today's applications and future developments of coatings for drills and rotating cutting tools, Surf. Coat. Technol. 76–77 (1995) 712–718.
[4] K. Bobzin, High-performance coatings for cutting tools, CIRP J. Manuf. Sci. Technol. 18 (2017) 1–9.
[5] B. Saha, W.Q. Toh, E. Liu, S.B. Tor, D.E. Hardt, J. Lee, A review on the importance of surface coating of micro/nano-mold in micro/nano-molding processes, J. Micromech. Microeng. 26 (2016), 013002/1-40.
[6] H.Y. Ueng, C.T. Guo, Diamond-like carbon coatings on microdrill using an ECR-CVD system, Appl. Surf. Sci. 249 (2005) 246–256.
[7] W.H. Kao, High-speed drilling performance of coated micro-drills with Zr–C:H:Nx% coatings, Wear 267 (2009) 1068–1074.
[8] P.A. Primeaux, B. Zhang, W.J. Meng, Performance of micro-drilling of hard Ni alloys using coated and uncoated WC/Co bits, Eng. Res. Express 1 (2019), 025046/1-10.
[9] J.C. Jiang, W.J. Meng, A.G. Evans, C.V. Cooper, Structure and mechanics of W-DLC coated spur gears, Surf. Coat. Technol. 176 (2003) 50–56.
[10] K.C. Mutyala, H. Singh, R.D. Evans, G.L. Doll, Deposition, characterization, and performance of tribological coatings on spherical rolling elements, Surf. Coat. Technol. 284 (2015) 302–309.
[11] ASTM Standard Procedure D4541 – 17, Standard Test Method for Pull-off Strength of Coatings Using Portable Adhesion Testers, ASTM International, 2017.
[12] J.M. Arenas, J.J. Narbon, C. Alia, Optimum adhesive thickness in structural adhesives joints using statistical techniques based on weibull distribution, Int. J. Adhes. Adhes. 30 (2010) 160–165.
[13] L.F.M. da Silva, R.D. Adams, Measurement of the mechanical properties of structural adhesives in tension and shear over a wide range of temperatures, J. Adhes. Sci. Technol. 19 (2005) 109–141.
[14] ASTM C1624-22, Standard Test Method for Adhesion Strength and Mechanical Failure Modes of Ceramic Coatings by Quantitative Single Point Scratch Testing.
[15] S.J. Bull, Can the scratch adhesion test ever be quantitative? Adhesion Measurement of Films and Coatings 2 (2001) 107.
[16] M.D. Drory, J.W. Hutchinson, Measurement of the adhesion of a brittle film on a ductile substrate by indentation, Proc. R. Soc. London A452 (1996) 2319–2341.
[17] D.C. Agrawal, R. Raj, Measurement of the ultimate shear strength of a metal/ceramic interface, Acta Metall. 37 (1989) 1265–1270.
[18] D.K. Leung, N.T. Zhang, R.M. McMeeking, A.G. Evans, Crack progression and interface debonding in brittle/ductile nanoscale multilayers, J. Mater. Res. 10 (1995) 1958–1968.
[19] M.D. Drory, J.W. Hutchinson, Diamond coatings of titanium alloys, Science 263 (1994) 1753–1755.
[20] B.F. Chen, J. Hwang, G.P. Yu, J.H. Huang, In situ observation of the cracking behavior of TiN coating on 304 stainless steel subjected to tensile strain, Thin Solid Films 352 (1999) 173–178.
[21] Y. Mu, K. Chen, B. Lu, W.J. Meng, G.L. Doll, Manufacturing of metal-based microparts: fabrication strategies and surface engineering applications, Surf. Coat. Technol. 237 (2013) 390–401.
[22] J.S. Wang, Y. Sugimura, A.G. Evans, W.K. Tredway, The mechanical performance of DLC films on steel substrates, Thin Solid Films 325 (1998) 163.
[23] K. Bewilogua, D. Hofmann, History of diamond-like carbon films — from first experiments to worldwide applications, Surf. Coat. Technol. 242 (2014) 214–225.
[24] C.A. Volkert, A.M. Minor, Focused ion beam microscopy and micromachining, MRS Bull. 32 (2007) 389–395.
[25] C. Jiang, H. Lu, H. Zhang, Y. Shen, Y. Lu, Recent advances on in situ sem mechanical and electrical characterization of low-dimensional nanomaterials, Scanning (2017), 1985149/1-11.
[26] D. Kiener, C. Motz, G. Dehm, R. Pippan, Overview on established and novel FIB based miniaturized mechanical testing using in-situ SEM, Int. J. Mat. Res. 100 (8) (2009) 1074–1087.
[27] J. Ast, M. Ghidelli, K. Durst, M. Goken, M. Sebastiani, A.M. Korsunsky, A review of experimental approaches to fracture toughness evaluation at the micro-scale, Mater. Des. 173 (2019), 107762/1-24.
[28] D. Di Maio, S.G. Roberts, Measuring fracture toughness of coatings using focused-ion-beam-machined microbeams, J. Mater. Res. 20 (2005) 299–302.
[29] K. Matoy, T. Detzel, M. Müller, C. Motz, G. Dehm, Interface fracture properties of thin films studied by using the micro-cantilever deflection technique, Surf. Coat. Technol. 204 (2009) 878–881.
[30] J.W. Hutchinson, Z. Suo, Mixed mode cracking in layered materials, Adv. Appl. Mech. 29 (1992) 63–191.
[31] A.G. Evans, J.W. Hutchinson, Y. Wei, Interface adhesion: effects of plasticity and segregation, Acta Mater. 47 (1999) 4093–4113.
[32] J. Schaufler, C. Schmid, K. Durst, M. Goken, Determination of the interfacial strength and fracture toughness of a-C: H coatings by in-situ microcantilever bending, Thin Solid Films 522 (2012) 480–484.
[33] W.J. Meng, T.J. Curtis, Inductively coupled plasma assisted physical vapor deposition of titanium nitride coatings, J. Electron. Mater. 26 (1997) 1297–1302.
[34] W.J. Meng, T.J. Curtis, L.E. Rehn, P.M. Baldo, Temperature dependence of inductively coupled plasma assisted growth of TiN thin films, Surf. Coat. Technol. 120 (121) (1999) 206–212.
[35] W.C. Oliver, G.M. Pharr, An improved technique for determining hardness and elastic modulus using load and displacement sensing indentation experiments, J. Mater. Res. 7 (1992) 1564–1583.
[36] B.X. Liu, X.Y. Cheng, A metastable CrC of NaCl structure formed by C-ion implantation into chromium films, J. Phys. Condens. Matter 4 (1992) L265–L268.
[37] S.M. Schmuecker, D. Clouser, T.J. Kraus, B.M. Leonard, Synthesis of metastable chromium carbide nanomaterials and their electrocatalytic activity for the hydrogen evolution reaction, Dalton Trans. 46 (2017) 13524–13530.
[38] W.J. Meng, T.J. Curtis, L.E. Rehn, P.M. Baldo, Plasma-assisted deposition and characterization of Ti-containing diamondlike carbon coatings, J. Appl. Phys. 83 (1998) 6076–6081.
[39] D.M. Cao, B. Feng, W.J. Meng, L.E. Rehn, P.M. Baldo, M.M. Khonsari, Friction and wear characteristics of ceramic nanocomposite coatings: titanium carbide/amorphous hydrocarbon, Appl. Phys. Lett. 79 (2001) 329–331.
[40] F. Iqbal, J. Ast, M. Goken, K. Durst, In situ micro-cantilever tests to study fracture properties of NiAl single crystals, Acta Mater. 60 (2012) 1193–1200.
[41] I. Issa, A. Hohenwarter, R. Fritz, D. Kiener, Fracture properties of ultrafine grain chromium correlated to single dislocation processes at room temperature, J. Mater. Res. 34 (2019) 2370–2383.
[42] X. Zhang, B. Zhang, Y. Mu, S. Shao, C.D. Wick, B.R. Ramachandran, W.J. Meng, Mechanical failure of metal/ceramic interfacial regions under shear loading, Acta Mater. 138 (2017) 224–236.
[43] X. Zhang, Y. Mu, M. Dodaran, S. Shao, D. Moldovan, W.J. Meng, Mechanical failure of CrN/Cu/CrN interfacial regions under tensile loading, Acta Mater. 160 (2018) 1–13.
[44] X. Zhang, R. Namakian, A.C. Meng, D. Moldovan, W.J. Meng, Size-dependent tensile failure of epitaxial TiN/Cu/TiN sandwich pillar structures: a combined experimentation – atomistic simulation study, Mater. Sci. Eng. A 855 (2022), 143889/1-11.
[45] Y.S. Kang, R.D. Evans, G.L. Doll, Contact mechanism of tribological coatings with columnar microstructure, in: STLE/ASME International Joint Tribology Conference Proceeding Paper, IJTC2008-71119, 2009, pp. 745–747.